J. Electrochem. Sci. Eng. **14(6)** (2024) 787-801; http://dx.doi.org/10.5599/jese.2409

Open Access : : ISSN 1847-9286
www.jESE-online.org

Original scientific paper

Electrochemical behavior and L-tyrosine sensing properties of nanostructured Cr, Sn and La-doped α-Fe_2O_3 interfaces

Kanza Maryam[1], Muhammad Umar Javed[1], Chanda Rafique[1], Amir Habib[2] and Adeel Afzal[1,✉]

[1]*Sensors and Diagnostics Lab, School of Chemistry, University of the Punjab, Quaid-i-Azam Campus, Lahore 54590, Pakistan*
[2]*Department of Physics, College of Science, University of Hafr Al Batin, PO Box 1803, Hafr Al Batin 39524, Saudi Arabia*

Corresponding authors: ✉ *adeel.chem@pu.edu.pk; Tel.: +92-313-913-8000*

Received: July 2, 2024; Accepted: October 26, 2024; Published: November 7, 2024

Abstract

L-tyrosine (Tyr) is a promising biomarker for the diagnosis and monitoring of metabolic disorders and neurodegenerative diseases. This study reports on the electrochemical properties of α-Fe_2O_3 nanostructures doped with Cr, Sn and La, referred to as $CrFeO_x$, $SnFeO_x$ and $LaFeO_x$, respectively, and their application in the enzyme-free electrochemical Tyr sensors. These disposable sensors offer accurate Tyr concentration analysis at room temperature, addressing the limitations of current point-of-care diagnostic methods. The $CrFeO_x$, $SnFeO_x$, and $LaFeO_x$ nanostructures serve as selective agents for binding and recognizing Tyr, deposited onto disposable graphite pencil electrodes to form the electrochemical interface. The interfacial resistance, charge-transfer kinetics, mechanism, and reversibility are studied via extensive electrochemical measurements employing electrochemical impedance spectroscopy and cyclic voltammetry. Furthermore, differential pulse voltammetry demonstrates excellent Tyr sensing performance in the concentration range of 0 to 80 μM with 2.65 μA $μM^{-1}$ cm^{-2} sensitivity and 360 nM threshold detection limit for the best-performing $CrFeO_x$ sensors. Hence, these α-Fe_2O_3-based sensor systems are practical and efficient for selective Tyr detection, offering potential advancements in personalized healthcare and early disease diagnosis.

Keywords

Metal doped ferric oxide; nonessential amino acid; biomarker; electrochemical sensors; point-of-care testing

Introduction

L-tyrosine (Tyr) is a nonessential α-amino acid involved in regulating protein synthesis and serves as the precursor for crucial neurotransmitters, including dopamine, and stress hormones, including adrenaline and noradrenaline [1]. Recent studies have reported significant advancements in the

electrochemical detection of these analytes [2-4]. The normal Tyr concentration in blood plasma ranges from 30-120 and 47 µM in saliva [5,6]. Significant variations in Tyr concentration may lead to adverse consequences such as depression, as well as the onset of different medical conditions, including alkaptonuria, albinism, Parkinson's disease, lung disorders, and liver ailments [7-9]. Thus, continuous monitoring of Tyr concentration is critical for the early detection and timely treatment of such diseases.

In this context, Dervin *et al*. [10] developed a disposable, wearable sensor based on graphene oxide-chitosan (GO-CS) composite-modified screen-printed carbon electrodes for point-of-care (POC) testing of Tyr. The GO-CS sensor revealed 5.86 µM Tyr detection limit (LOD). Xu *et al*. [11] also prepared a wearable electrochemical Tyr sensor using a tannic acid-silver-carbon nanotubes-polyaniline (TA-Ag-CNT-PANI) composite hydrogel and achieved 3.3 µM LOD. The sensor could simultaneously monitor pH and Tyr in sweat. Recently, Vaughan *et al*. [12] reported a graphene-based electrochemical Tyr sensor with a slightly improved LOD, *i.e*., 3.03 µM. Hence, the development of a reliable, cost-effective sensor for Tyr recognition, especially at sub-micromolar levels, is vital for POC diagnostics, and significant efforts are underway to address this challenge.

In this work, the synthesis and Tyr-sensing properties of variously-doped α-Fe_2O_3 nanoparticles such as $CrFeO_x$, $SnFeO_x$, and $LaFeO_x$ are investigated, with a primary objective of realizing sub-micromolar Tyr-LOD and high sensitivity. Metal-doped iron oxides are highly robust, magnetic nanomaterials with excellent electronic properties [13]. In this case, they contain Fe^{3+}, Cr^{3+}, Sn^{4+}, and La^{3+} ions, which are intrinsic hard acids and can promote the recognition of hard bases, *e.g*., Tyr, through affinity interactions. Furthermore, α-Fe_2O_3 is often a material of choice for preparing composite nanostructures and sensing biologically relevant analytes and inorganic gases due to its excellent electronic properties [14-16]. Hence, the $CrFeO_x$, $SnFeO_x$, and $LaFeO_x$ sensors are purposefully developed with high sensitivity, selectivity, and sub-micromolar LOD for future POC diagnostics to monitor metabolic disorders and neurodegenerative diseases.

Experimental

Synthesis of $MFeO_x$ nanostructures

$CrFeO_x$, $SnFeO_x$, and $LaFeO_x$ nanostructures were synthesized using a sol-gel method [17]. Initially, a clear and homogeneous solution was prepared by dissolving 2.7 grams of $FeCl_3{\cdot}6H_2O$ (≥99 %, SigmaAldrich) and 5 mol.% of either $CrCl_3{\cdot}6H_2O$ (≥99 %, Sigma Aldrich), $SnCl_4{\cdot}5H_2O$ (≥97 %, BDH Chemicals Ltd.) or $LaCl_3{\cdot}7H_2O$ (≥97 %, UNI-Chem Ltd.) in 100 mL of deionized water. To stabilize the colloidal solution, 125 mg of polyvinyl alcohol (PVA, Sigma Aldrich) was added, and the mixture was stirred at 60 °C for an hour. The solution pH was adjusted to a basic level (pH = 8) by carefully adding 25 % liquid ammonia (NH_3, Sigma Aldrich), followed by four hours of stirring to ensure uniformity. The resulting slurry was then subjected to centrifugation to isolate a brown-colored product, which underwent thorough washing with deionized water for impurity removal. Subsequently, $CrFeO_x$, $SnFeO_x$, and $LaFeO_x$ nanomaterials were dried at 70 °C, followed by calcination at 800 °C for four hours to induce crystallization and enhance material properties. Finally, the obtained products were ground into a fine powder using a mortar and pestle and characterized experimentally.

Characterization

All samples were characterized using an Agilent Cary 630 Fourier-transform infrared (FTIR) spectrophotometer, Shimadzu LabX XRD-6100 X-ray diffractometer, and FEI Inspect^{TM} S50 scanning electron microscope (SEM).

Fabrication of electrochemical Tyr sensors

To construct electrochemical Tyr sensors, graphite pencil electrodes (GPEs, 0.7 mm diameter and 6 cm length) were first cleaned with ethanol, acetone, and deionized water. Multiple Tyr sensors were fabricated by dip coating a 3 cm portion of GPEs with a suspension of $CrFeO_x$, $SnFeO_x$, and $LaFeO_x$ nanopowders, as shown in Figure 1. For immobilization of $CrFeO_x$, $SnFeO_x$, and $LaFeO_x$ nanostructures and subsequent fabrication, a Tyr-imprinted hyper-crosslinked polymer was synthesized *via* a reported procedure [18], while employing Tyr as the template. $MFeO_x$ could be dispersed in water and alcohol but did not form a stable coating on the GPE surface. Hence, for fabrication purposes, $MFeO_x$ nanostructures were immobilized in a Tyr-imprinted polymer (Figure 1A), which offered the formation of stable suspensions and coatings on the GPE surface. $CrFeO_x$, $SnFeO_x$, and $LaFeO_x$ nanostructures (1 mg mL^{-1}) were suspended in this polymer solution and dip-coated on GPEs. The devices were subsequently dried at 70 °C and were stored in a closed container. All devices were thoroughly washed with deionized water before electrochemical analysis.

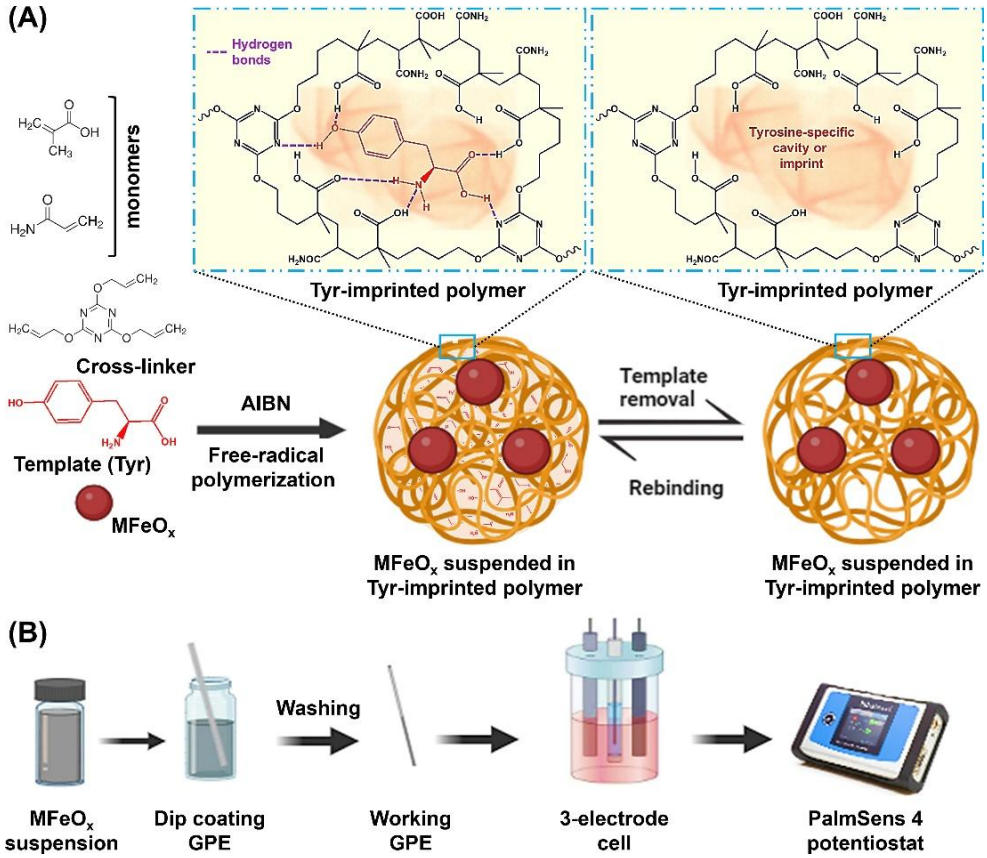

Figure 1. *Fabrication of $MFeO_x$/GPE-based voltammetric sensors: (A) formation of a Tyr-imprinted polymer as an immobilization matrix for $MFeO_x$ nanostructures to create stable MFeOx suspension and coatings on GPE, and (B) dip-coating procedure and electrochemical measurement setup ($MFeO_x$: M, i.e., Cr, Sn, and La-doped α-Fe_2O_3 nanostructures; GPE: graphite pencil electrode)*

Electrochemical sensor measurements

The electrochemical measurements were conducted using a portable PalmSens4 single-channel Potentiostat, acquired from PalmSens BV, The Netherlands, and operated by the PSTrace v5.8 software. A three-electrode system was utilized, as shown in Figure 1b, comprising a modified GPE as the working electrode, a standard Ag/AgCl (3 M KCl) electrode as the reference electrode, and a platinum wire electrode as the counter electrode. Firstly, the fabricated sensors were characterized by electrochemical impedance spectroscopy (EIS, using a PalmSens 4 potentiostat, AC

amplitude: 0.006 V, frequency range: 100 kHz to 1 Hz, at 0.1 V) to determine the properties of the respective polymeric coatings.

For studying the electrochemical response of fabricated sensors to different concentrations of Tyr, cyclic voltammetry (CV) and differential pulse voltammetry (DPV) were used. To create a standard redox solution, equimolar concentrations (2.5 mM) potassium hexacyanoferrate (II) trihydrate ($K_4[Fe(CN)_6]\cdot 3H_2O$, ACS reagent, 98.5-102.0 %, Sigma Aldrich), and potassium hexacyanoferrate (III) ($K_3[Fe(CN)_6]$, ACS reagent, ≥99.0 %, Sigma Aldrich) were dissolved in a phosphate buffer saline (PBS, pH 7.4, locally obtained PBS tablets). Subsequently, 1 to 80 µM Tyr solutions were prepared in the same PBS standard redox solution. Cyclic voltammetry (CV) measurements were conducted within a potential range of -0.8 to +0.8 V at a scan rate of 100 mV s^{-1}.

Additionally, the impact of varying scan rates (ranging from 10 to 100 mV s^{-1}) on the electrochemical results was investigated. DPV measurements were recorded in the range of -0.8 to +0.8 V at a scan rate of 100 mV s^{-1}. The sensor responses were determined through CV and DPV analyses focusing on the peak current shifts during the oxidation/reduction of $[Fe(CN)_6]^{3-/4-}$ in PBS. To ensure accuracy, all measurements were carried out in triplicate at a minimum, and the mean values along with the standard deviation, were reported. To assess selectivity, solutions containing 80 µM of various interfering analytes, including urea, creatinine, uric acid, cysteine, ascorbic acid, *etc.*, were prepared within the standard redox solution and subsequently tested using the Tyr sensors.

Results and discussion

Characterization

$CrFeO_x$, $SnFeO_x$, and $LaFeO_x$ nanostructures were synthesized *via* a facile sol-gel process using poly(vinyl alcohol) as a stabilizer and thermally calcined at 800 °C to fabricate three different sensors. Fourier-transform infrared (FTIR) spectra, shown in Figure 2A-C, do not reveal the presence of alkyl groups of PVA or other organic functional groups, thereby confirming the formation of inorganic $MFeO_x$ nanostructures.

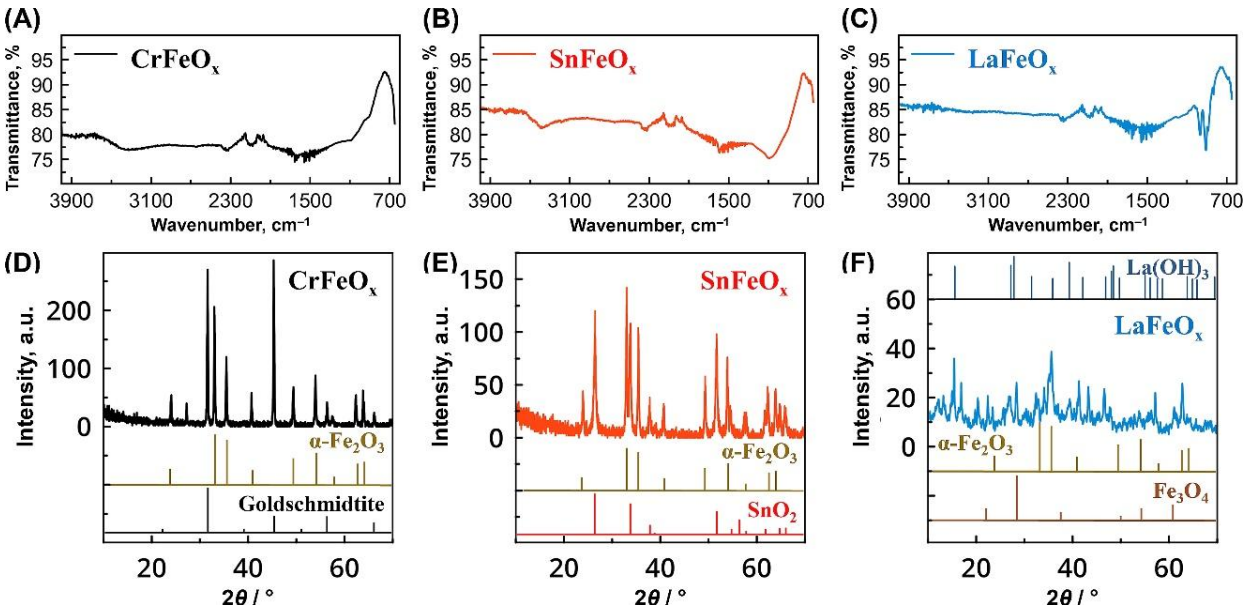

Figure 2. *(A-C) FTIR spectra, and (D-F) XRD patterns of (A, D) $CrFeO_x$, (B, E) $SnFeO_x$, and (C, F) $LaFeO_x$ nanocrystals. The bottom inserts in (D-F) show reference XRD patterns of matching crystallite phases*

FTIR spectra show a weak absorption band at approximately 2200 to 2400 cm^{-1} attributed to atmospheric CO_2 [19]. $CrFeO_x$, $SnFeO_x$, and $LaFeO_x$ spectra were quite similar with characteristic

absorption bands at 3300 to 3400 and 1627 cm^{-1}, corresponding to the stretching and bending vibration of coordinated water molecules adsorbed from the atmosphere and surface -OH moieties [20,21]. The peaks around 650 cm^{-1} are attributed to the M-O bonds in $MFeO_x$ samples [22].

Figure 2D-F shows the X-ray diffraction (XRD) patterns of $MFeO_x$ nanocrystals. The presence of rhombohedral α-Fe_2O_3 or hematite phase (JCPDS 79-0007 [23,24]) is detected in the XRD patterns of all $MFeO_x$ samples, along with a mix of other phases. In particular, the XRD pattern of $CrFeO_x$ exhibits the cubic, perovskite-type goldschmidtite phase, corresponding to the Pm-3m space group (COD 96-156-5135 [25]). $SnFeO_x$ sample shows the existence of a tetragonal, rutile SnO_2 phase (JCPDS 71-0652 [26]) in addition to α-Fe_2O_3. On the other hand, α-Fe_2O_3, Fe_3O_4 (JCPDS 19-0629 [27]), and impurities such as $La(OH)_3$ (JCPDS 06-0585 [28]) are detected in the XRD pattern of the $LaFeO_x$ sample, which shows poor crystallinity compared to $CrFeO_x$ and $SnFeO_x$ nanocrystals.

Scanning electron micrographs (SEM) of $CrFeO_x$, $SnFeO_x$, and $LaFeO_x$ nanostructures are presented in Figure 3.

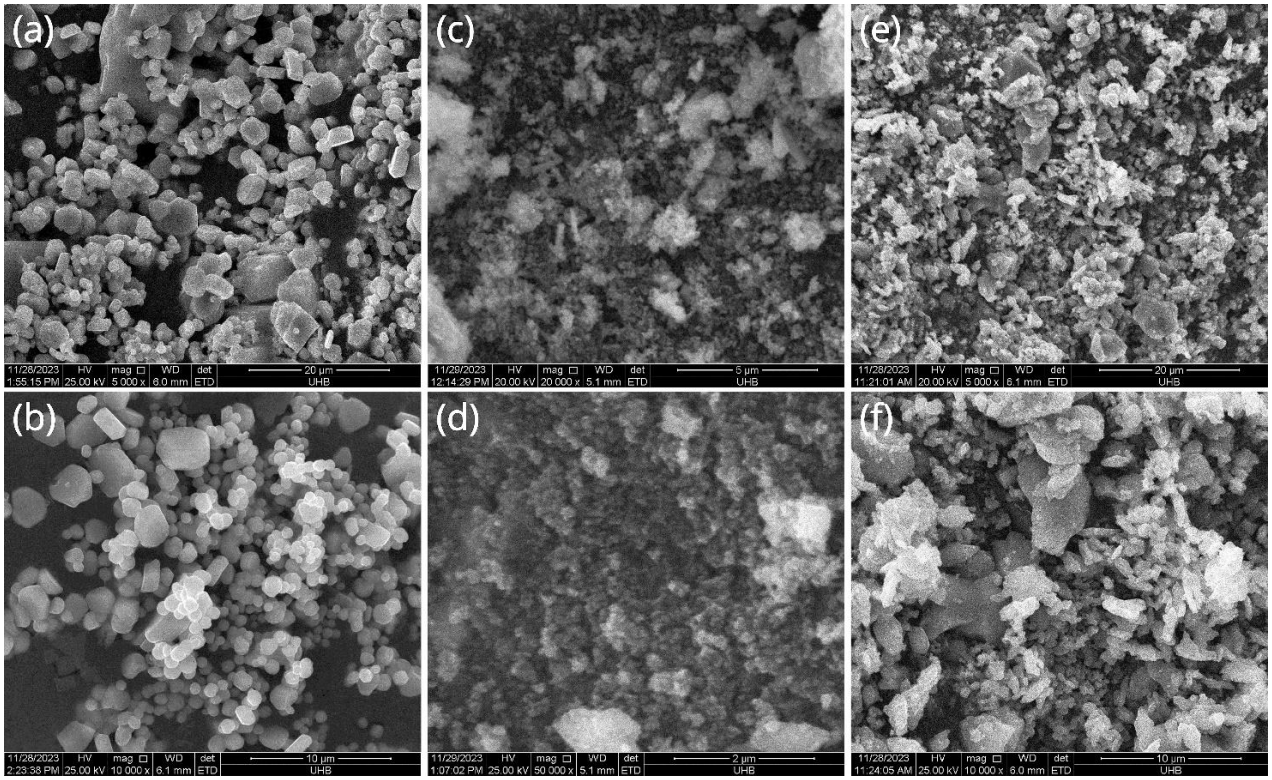

Figure 3. *SEM images of (a, b) $CrFeO_x$, (c, d) $SnFeO_x$, and (e, f) $LaFeO_x$ nanostructures at different magnifications*

All $MFeO_x$ samples exhibit distinct surface morphology and microstructure. $CrFeO_x$ (Figure 3a-b) presents agglomerates of nanoparticles of varying size and shape, depicting the presence of more than one type (phase) of crystals. $SnFeO_x$ (Figure 3c-d) shows a nanostructured surface with clusters of nanoscale particles, uniformly dispersed along the surface. $LaFeO_x$ (Figure 3e to 3f), on the other hand, demonstrates microscale clumps, particles, and rod-like morphologies, again depicting a mixture of distinct phases (crystallites). Hence, XRD and SEM results confirm the formation of diverse types of $MFeO_x$ nanostructures, all produced *via* a similar PVA-stabilized sol-gel process. It also emphasizes the effects of various metal ions (Cr^{3+}, Sn^{4+}, and La^{3+}) doping on the evolution of $MFeO_x$ nanostructures, which in turn may influence their electrochemical characteristics and sensor properties.

Electrochemical behavior

Figure 4 presents the EIS analysis of the $MFeO_x$ nanocomposite sensors. The respective Nyquist and Bode plots demonstrate the electrochemical features of $CrFeO_x$, $SnFeO_x$, and $LaFeO_x$ sensors. The electron-transfer resistance at the electrode-electrolyte interface (R_{ct}) is measured as 225, 347, and 653 Ω for $CrFeO_x$, $SnFeO_x$, and $LaFeO_x$ sensors, respectively. The measured R_{ct} value plays a critical role in governing electron transfer dynamics at the interface, where a lower R_{ct} value suggests faster electron transfer kinetics [29]. The reduction in R_{ct} of $CrFeO_x$-modified electrodes can be attributed to the effective attachment and increased electroactive surface area of the $CrFeO_x$ nanocomposite, creating pathways for more efficient charge transfer [30]. The absolute impedance values at medium to low frequencies are also the lowest for $CrFeO_x$-modified electrodes, as shown in Bode magnitude plots (Figure 4C). In addition, Bode magnitude and Bode phase angle plots (Figure 4D) suggest a higher degree of charge storage or capacitance for $CrFeO_x$ compared to $SnFeO_x$ and $LaFeO_x$. It is attributed to the different ability of dopants to separate and store charge at the electrode-electrolyte interface.

CV results also show higher oxidation and reduction peak currents for $CrFeO_x$-modified electrodes compared to $SnFeO_x$ and $LaFeO_x$, which is attributed to its exceptional electrocatalytic characteristics and larger electroactive surface area, as determined from the Randles-Ševčík equation (1) for a quasi-reversible process [31].

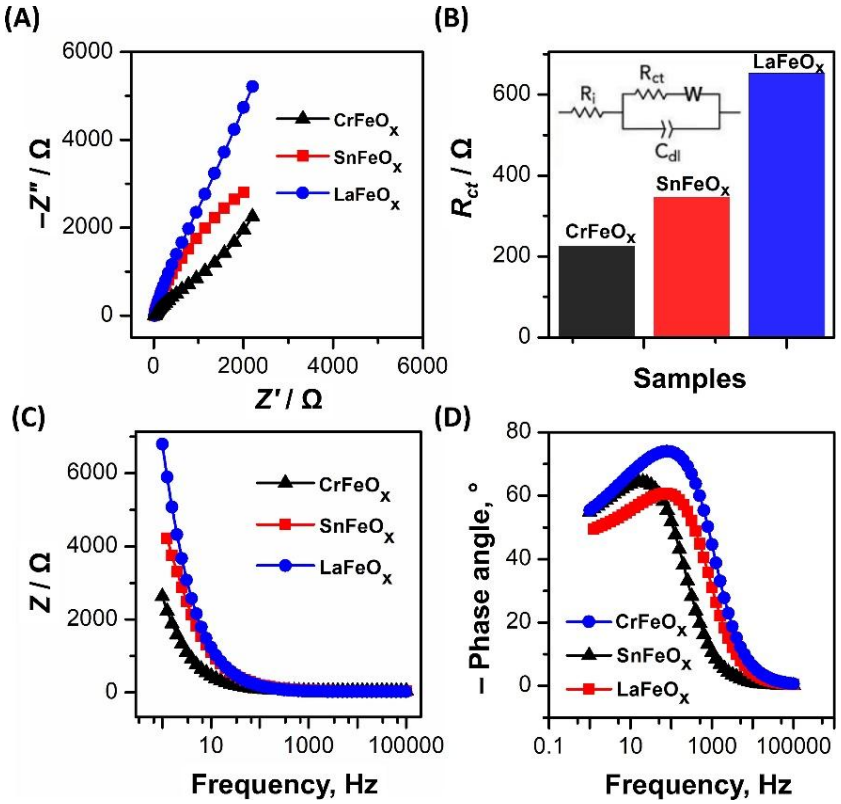

Figure 4. *EIS analysis: (A) Nyquist plots, (B) corresponding R_{ct} values (obtained by fitting Randles circuit shown in the inset, to the EIS data), (C) Bode magnitude plots, and (D) Bode phase angle plots. EIS measurements are performed in a standard redox solution under ambient conditions at pH 7.4 and a frequency range of 100,000-1 Hz.*

$$I_{pa} = 0.436\,nFCA_{real}\sqrt{\frac{nFDv}{RT}} \quad (1)$$

I_{pa} / A is the anodic peak current, n is the number of electrons involved, F is Faraday constant (96485 C mol^{-1}), C / mol cm^{-3} is the concentration of $[Fe(CN)_6]^{3-/4-}$, A_{real} / cm^2 is the electroactive surface

area of the electrode, D / cm^2 s^{-1} is the diffusion coefficient, v / V s^{-1} is the voltammetric scan rate, R is the universal gas constant (8.314 J Kmol^{-1}), and T / K is operating temperature. The calculated electroactive area of the $CrFeO_x$, $SnFeO_x$, and $LaFeO_x$ electrodes are 0.342, 0.392 and 0.330 cm^2, respectively. Similarly, the heterogeneous rate constant (K^o), representing the electron transfer kinetics, is calculated according to equation (2) [32,33].

$$K° = RT / R_{ct}ACF^2 \quad (2)$$

The calculated $K°$ for the bare electrode is 2.22×10^{-4} cm s^{-1}, while for $CrFeO_x$, $SnFeO_x$, and $LaFeO_x$ electrodes, $K°$ is 1.38×10^{-3}, 7.82×10^{-4} and 4.94×10^{-4} cm s^{-1}, respectively, which are either comparable or an order of magnitude than the reported $K°$ values for α-Fe_2O_3 nanostructures [34]. The higher heterogeneous rate constant observed for the $CrFeO_x$ sensor can primarily be attributed to its higher conductivity and fast electron transfer kinetics at the electrode-electrolyte interface. Again, these results are consistent with the earlier observations from the EIS measurements.

The roughness factor (f_r) quantifies the surface roughness of an electrode and is the ratio of anodic peak currents or the electroactive area of the modified and bare electrodes. It is determined by the following equation (3) [35]:

$$f_r = I_{p2} / I_{p1} = A_2 / A_1 \quad (3)$$

In this context, I_{p2} represents the anodic peak current of the modified electrode, while I_{p1} denotes the anodic peak current of the bare electrode. Similarly, A_2 signifies the electroactive area of the modified electrodes, and A_1 refers to the electroactive area of the bare electrode, *i.e.,* 0.2 cm^2. The roughness factor for $CrFeO_x$, $SnFeO_x$ and $LaFeO_x$-modified electrodes are 1.71, 1.96 and 1.65, respectively. This is attributed to the different composition of nanocomposites and their surface properties.

Electrochemical Tyr sensing mechanisms

The electrochemical Tyr-sensing mechanism is also evaluated by CV scans at different scan rates (0.01-0.10 V s^{-1}). Figure 5 depicts the impact of the scan rate on the oxidation peak current (I_{pa}) of different sensors. As the scan rate varies from 0.01 to 0.10 V s^{-1}, a rise in the I_{pa} of the $MFeO_x$ sensors is observed. Thereby, a linear relationship between the I_{pa} and square root of the scan rate ($v^{½}$) is established, indicating the prevalence of diffusion-limited electrochemical redox reactions at the sensor surface [36,37]. The redox processes at the electrode surface demonstrate reversible behavior since the measurements are conducted in a standard redox solution containing $[Fe(CN)_6]^{3-/4-}$ redox probe. However, the broader peaks and the greater peak separations indicate a drop in electron transfer efficiency and a shift toward quasi-reversible behavior. The corresponding linear regression equations (4) to (6) are defined as follows:

$CrFeO_x$; $I_{pa} = (14.39 \pm 0.435)\, v^{½} - (6.166 \pm 0.185)$; ($R^2 = 0.991$) (4)

$SnFeO_x$; $I_{pa} = (11.18 \pm 0.281)\, v^{½} - (6.734 \pm 0.197)$; ($R^2 = 0.994$) (5)

$LaFeO_x$; $I_{pa} = (14.38 \pm 0.385)\, v^{½} - (6.394 \pm 0.215)$; ($R^2 = 0.993$) (6)

Figure 6A to 6-C shows the correlation between the logarithm of anodic peak current (I_{pa}) and the logarithm of scan rate (v), to further support the diffusion-controlled process as presented in the following equations (7) to (9):

$CrFeO_x$: $\log I_{pa} = (0.49 \pm 0.0190) \log v - (1.395 \pm 0.018)$; ($R^2 = 0.99$) (7)

$SnFeO_x$: $\log I_{pa} = (0.48 \pm 0.0049) \log v + (0.722 \pm 0.008)$; ($R^2 = 0.98$) (8)

$LaFeO_x$: $\log I_{pa} = (0.45 \pm 0.0071) \log v - (1.360 \pm 0.011)$; ($R^2 = 0.99$) (9)

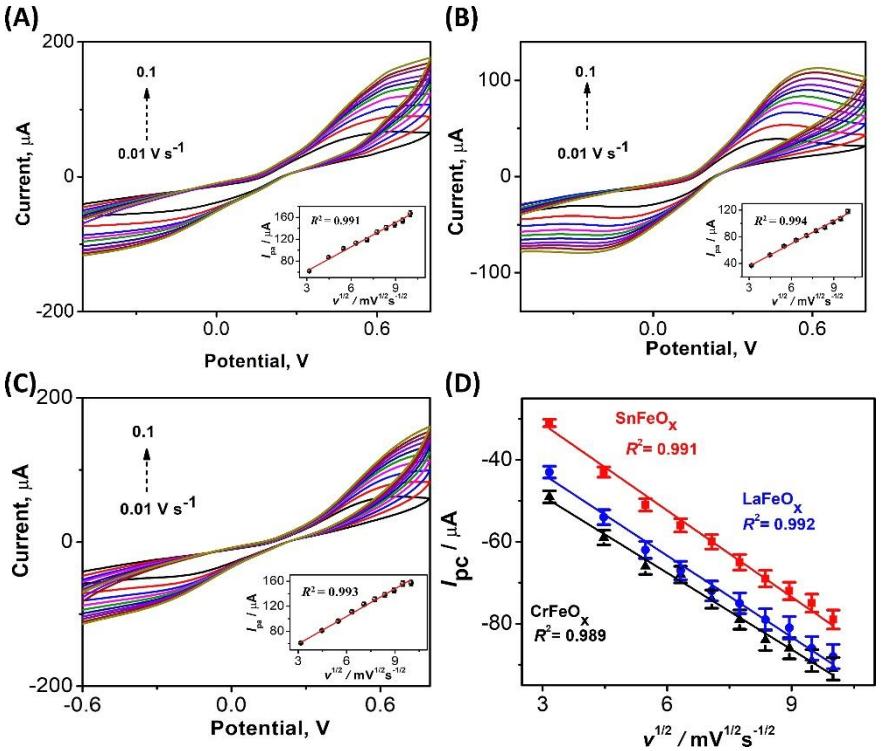

Figure 5. *CV scans of (A) $CrFeO_x$, (B) $SnFeO_x$, and (C) $LaFeO_x$-modified electrodes in a standard redox solution at different scan rates (0.01-0.10 V s^{-1}). The respective plots of anodic or oxidation peak current (I_{pa}) vs. square root of the scan rate ($v^{½}$) are shown in the insets. (D) The respective plots of cathodic or reduction peak currents (I_{pc})* vs. $v^{½}$. *All measurements are conducted in a standard redox solution under ambient conditions at pH 7.4*

The slope value observed in the plot of log I_{pa} *vs.* log *v* serves as an indicator of the following mechanism, with a value of 0.5 suggestive of a diffusion-controlled process, while a value of 1.0 suggests an adsorption-controlled process. For $CrFeO_x$, $SnFeO_x$, and $LaFeO_x$ sensors, the obtained slope values are 0.49, 0.48, and 0.45, respectively, closely approximating the theoretically predicted value of 0.5 [30]. This coherence demonstrates that the redox reaction taking place at the electrode predominantly follows a diffusion-controlled mechanism, with limited adsorption transpiring at the electrode surface.

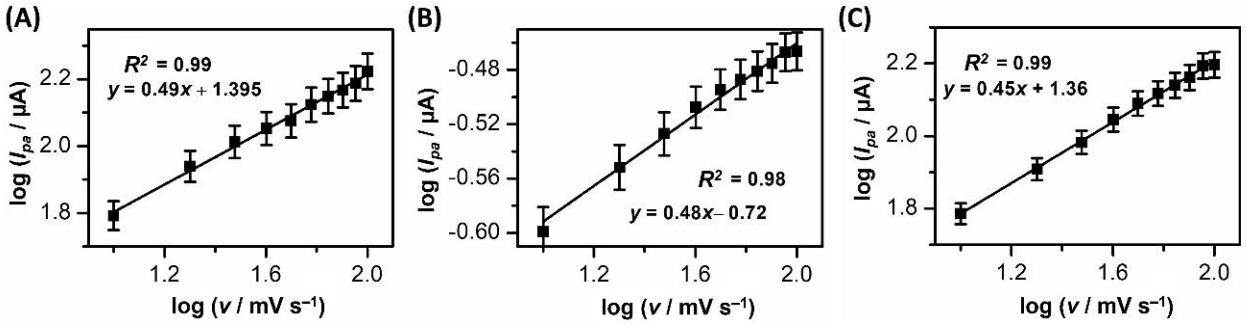

Figure 6. *The log Ipa plotted against the log of scan rate for (A) $CrFeO_x$, (B) $SnFeO_x$, and (C) $LaFeO_x$ sensors*

Electrochemical Tyr sensing properties

Figure 7 shows CV responses of the $CrFeO_x$, $SnFeO_x$, and $LaFeO_x$ sensors as a function of varying Tyr concentrations (0-80 µM). A gradual decrease in current (I_{pa}) is observed with an increase in Tyr concentration, which is primarily due to the competitive binding and blocking effect associated with the imprinted polymer layer, which selectively binds tyrosine on the sensor surface. As tyrosine concentration increases, more tyrosine molecules bind to the specific sites in the imprinted polymer,

effectively "blocking" the surface. This blockage restricts the access of $[Fe(CN)_6]^{4-/3-}$ ions to the electrode, reducing the extent of the electron transfer reaction reflected in the decreased peak current. The corresponding calibration curves of the $CrFeO_x$, $SnFeO_x$, and $LaFeO_x$ sensors exhibit a straight line with a negative slope and R^2 values approaching approximately 1, as shown in Figure 5, expressing a high degree of linearity in the measured Tyr concentration range.

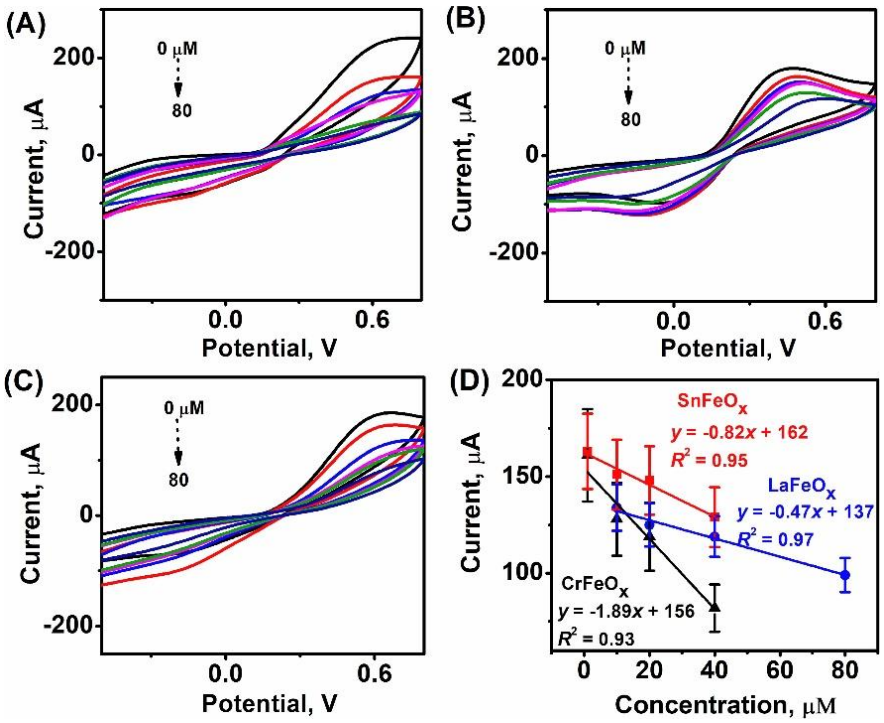

Figure 7. *CV response of (A) $CrFeO_x$, (B) $SnFeO_x$, and (C) $LaFeO_x$ sensors toward different concentrations of Tyr (0-80 µM) in a standard redox solution; (D) the corresponding calibration curves show the oxidation peak currents as a function of Tyr concentration. All measurements are conducted in standard redox solutions with varying Tyr concentrations under ambient conditions at pH 7.4 and scan rate of 0.10 V s^{-1}*

Furthermore, DPV measurements were conducted to comprehensively assess and validate the electrochemical sensor performance. These measurements serve the purpose of determining sensitivity as well as establishing LOD and LOQ. Figure 8 presents the DPV response of the $CrFeO_x$, $SnFeO_x$, and $LaFeO_x$ sensors. A gradual decline in DPV current is observed as the concentration of Tyr increases from 0-80 µM, owing to the occupation and saturation of the available active sites on the $MFeO_x$ sensor surface with Tyr molecules, leading to an increase in effective resistance and a decrease in peak current. The corresponding calibration curves (current density *vs*. Tyr concentration plots) of different sensors establish a linear relationship, with R^2 values in the range of 0.92-0.95. DPV is a very sensitive technique, and small changes in analyte concentration could significantly affect current changes. On the other hand, the uniformity of the electrode surface at the nanoscale and its thickness impact the sensor response. Nonetheless, the errors obtained from the standard deviation of measurements (performed in triplicate, at least) are within the permissible limits. DPV measurements demonstrate the highest sensitivity (2.65 µA cm^{-2} $µM^{-1}$) for $CrFeO_x$, while LOD and LOQ are determined to be 0.36 and 1.09 µM, respectively. The $CrFeO_x$ nanocomposite sensor exhibits exceptional properties that surpass $SnFeO_x$ and $LaFeO_x$ sensors, primarily attributable to the remarkable conductivity of Cr-doped α-Fe_2O_3 nanostructures and electrochemical features of $CrFeO_x$ nanocomposite, as discussed earlier. These sensor properties are well-suited for the envisioned use of these sensors in the context of salivary Tyr diagnosis.

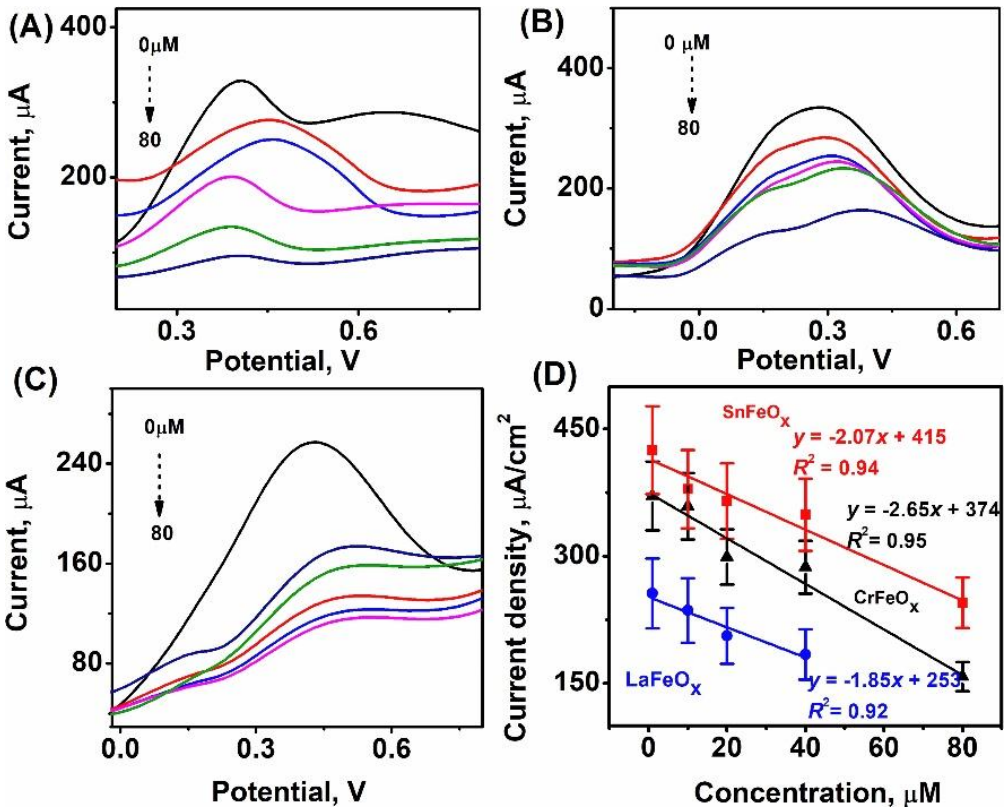

Figure 8. *DPV response of (A) $CrFeO_x$, (B) $SnFeO_x$, and (C) $LaFeO_x$ sensors toward different concentrations of Tyr (0-80 μM) in a standard redox solution; (D) the corresponding calibration curves show variations in the oxidation peak currents as a function of Tyr concentration. All measurements are conducted in standard redox solutions with varying Tyr concentrations under ambient conditions at pH 7.4 and a scan rate of 0.10 V s^{-1}*

In the field of point-of-care (POC) diagnostics and real-world applications, however, the selectivity of an electrochemical sensor is of paramount concern. In this context, the cross-sensitivity of the best-performing $CrFeO_x$ sensors against several interferents, including ascorbic acid, creatinine, cysteine, glutamine, urea, and uric acid, is determined. Figure 9 shows the cross-sensitivity data.

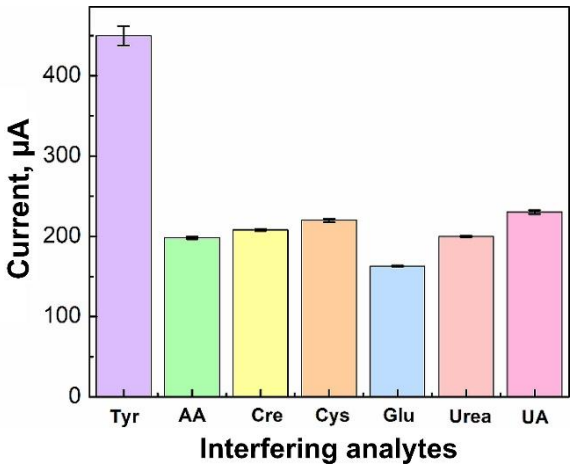

Figure 9. *The selectivity of the $CrFeO_x$ Tyr sensor: normalized current response of the $CrFeO_x$ sensor toward 80 μM of various analytes - Tyr: tyrosine, AA: ascorbic acid, Cre: creatinine, Cys: cysteine, Glu: glutamine, and UA: uric acid - in standard redox solutions*

The results indicate that the $CrFeO_x$ sensor exhibits remarkable selectivity, partly attributed to its intrinsic hard-acid-hard-base interactions and partly to the Tyr-imprinted immobilization matrix. The $CrFeO_x$ sensor exhibits complementary binding sites for Tyr, offering greater Tyr selectivity and lower cross-sensitivity toward various interferents.

Comparison of electrochemical Tyr sensor performance

The results of this work are compared with recently published examples from the relevant literature to evaluate the performance of $CrFeO_x$, $SnFeO_x$ and $LaFeO_x$ sensors, and the data are presented in Table 1. Note that comparison is only tentative due to the presentation of most results in the form not specified to the electrode surface area term. Among these examples of electrochemical Tyr sensors in Table 1, $CrFeO_x$ reveals very high sensitivity. LOD is also in the nanomolar range, which is good enough from a practical point of view, as the normal concentrations of Tyr in physiological fluids are found to be in the micromolar range.

Table 1. *Performance comparison of sensors for Tyr detection developed in this work with those already documented in the literature*

Material	Methods	Detection range, µM	LOD, µM	Sensitivity,µA μM^{-1} * µA μM^{-1} cm^{-2}	Ref.
GO/chitosan	CV, DPV	1-100	5.86	0.0846	[10]
Graphene	SWV	5-250	3.03	0.018	[12]
Graphene/chitosan	SD-LSV	0.006-0.8; 0.8-10	0.004	-	[38]
Carbon black NPs	CV, DPV, SWV	30-500	4.4	-	[39]
MXene/CNTs/CuMOF	CV, DPV	0.53-232.46	0.19	-	[40]
Cu^{II}-MOF	DPV	10-90	5.82	-	[41]
Graphene/Au NPs	CV, LSV	0.1-100	0.047	0.918	[42]
Graphene	CV, LSV	6-6000	1.81	0.0124	[43]
Al-CuSe NPs	CV, LSV	0.15-10	0.04	-	[44]
MWCNTs-Nafion	CV, DPV	2.0-120.0	0.8	-	[45]
Poly(p-toluenesulfonic acid)	SWV	1-70	0.210	-	[46]
Polypyrrole/FeCN	CV	0.5-27	0.082	1.46	[47]
rGO/AB/paste electrode	CV	0.1-100	0.06	3.31*	[30]
$CrFeO_x$	CV, DPV	0-80	0.359	2.65*	This work
$SnFeO_x$			0.402	2.07*	
$LaFeO_x$			0.531	1.85*	

Compared to previous studies, the competitive advantages of this work lie in the ease of electrode fabrication, cost-effectiveness, and enhanced selectivity of the $CrFeO_x$/GPE sensors. GPEs used in this work are extremely economical as they cost less than 0.1 $ per electrode. It is apparent that the $CrFeO_x$ sensors demonstrate exceptional electrochemical sensing capabilities, showcasing superior sensitivity, a broader linear detection range, and a lower LOD in comparison to other existing electrochemical devices for non-enzymatic Tyr detection. By enabling rapid and accurate measurement, this $CrFeO_x$ sensor holds significant potential for the detection of Tyr.

Conclusions

The facilitation of early disease detection at a reduced cost is crucial for ensuring accessible healthcare worldwide. This work was focused on the development of highly sensitive point-of-care (POC) diagnostic sensors to enable the timely identification of Tyr (a biomarker associated with various medical conditions). The sensors were based on Cr/Sn/La-doped α-Fe_2O_3 nanostructures immobilized in a Tyr-imprinted polymer and integrated with cost-efficient GPEs, and comprehensively characterized using a range of advanced techniques. The analysis conducted by EIS and CV revealed a diffusion-controlled redox process occurring at the $CrFeO_x$ surface, facilitating uninterrupted charge transfer. Additionally, CV and DPV measurements demonstrated remarkable sensor properties. In particular, DPV analysis demonstrates a linear response to Tyr in a concentration range of 0 to 80 µM

and a LOD in the sub-micromolar range. Notably, these measurements have revealed enhanced sensor properties for the $CrFeO_x$ sensor, making it highly suitable for real-time analysis and practical implementation in POC diagnostics. The CrFeOx Tyr sensors could potentially be integrated into wearable devices for healthcare monitoring through increased sensitivity, miniaturization, and integration with mobile or wearable technologies.

Conflict of Interest: The authors declare no competing financial interests.

Acknowledgements*:* A. Afzal gratefully acknowledges the University of Hafr Al Batin and the Ministry of Education, KSA for the provision of research facilities and continuous support.

Contribution: K. Maryam, M. U. Javed and C. Rafique contributed equally to the experimental work.

References

[1] Y. Yang, Y. Song, X. Bo, J. Min, O. S. Pak, L. Zhu, M. Wang, J. Tu, A. Kogan, H. Zhang, T. K. Hsiai, Z. Li, W. Gao, A laser-engraved wearable sensor for sensitive detection of uric acid and tyrosine in sweat, *Nature Biotechnology* **38** (2020) 217-224. https://doi.org/10.1038/s41587-019-0321-x

[2] S. Biswas, H. Naskar, S. Pradhan, Y. Wang, R. Bandyopadhyay, P. Pramanik, Simultaneous voltammetric determination of Adrenaline and Tyrosine in real samples by neodymium oxide nanoparticles grafted graphene, *Talanta* **206** (2020) 120176. https://doi.org/10.1016/j.talanta.2019.120176

[3] S. K. Revanappa, I. Soni, M. Siddalinganahalli, G. K. Jayaprakash, R. Flores-Moreno, C. Bananakere Nanjegowda, A Fukui Analysis of an Arginine-Modified Carbon Surface for the Electrochemical Sensing of Dopamine, *Materials* **15** (2022) 6337. https://doi.org/10.3390/ma15186337

[4] R. S. Kumar, G. K. Jayaprakash, S. Manjappa, M. Kumar, A. P. Kumar, Theoretical and electrochemical analysis of L-serine modified graphite paste electrode for dopamine sensing applications in real samples, *Journal of Electrochemical Science and Engineering* **12** (2022) 1243-1250. https://doi.org/10.5599/jese.1390

[5] Z. T. Dame, F. Aziat, R. Mandal, R. Krishnamurthy, S. Bouatra, S. Borzouie, A. C. Guo, T. Sajed, L. Deng, H. Lin, P. Liu, E. Dong, D. S. Wishart, The human saliva metabolome, *Metabolomics* **11** (2015) 1864-1883. https://doi.org/10.1007/s11306-015-0840-5

[6] V.C. Valsalakumar, A.S. Joseph, J. Piyus, S. Vasudevan, Polyaniline-Graphene Oxide Composites Decorated with ZrO2 Nanoparticles for Use in Screen-Printed Electrodes for Real-Time l-Tyrosine Sensing, *ACS Applied Nano Materials* **6** (2023) 8382-8395. https://doi.org/10.1021/acsanm.3c00659

[7] J. B. Mistry, M. Bukhari, A. M. Taylor, Alkaptonuria, *Rare Diseases* **1** (2013) e27475. https://doi.org/10.4161/rdis.27475

[8] D. Banik, S. Kundu, P. Banerjee, R. Dutta, N. Sarkar, Investigation of Fibril Forming Mechanisms of l-Phenylalanine and l-Tyrosine: Microscopic Insight toward Phenylketonuria and Tyrosinemia Type II, *Journal of Physical Chemistry B* **121** (2017) 1533-1543. https://doi.org/10.1021/acs.jpcb.6b12220

[9] Z. D. Zhou, W. T. Saw, P. G. H. Ho, Z. W. Zhang, L. Zeng, Y. Y. Chang, A. X. Y. Sun, D. R. Ma, H. Y. Wang, L. Zhou, K. L. Lim, E.-K. Tan, The role of tyrosine hydroxylase-dopamine pathway in Parkinson's disease pathogenesis, *Cellular Molecular Life Sciences* **79** (2022) 599. https://doi.org/10.1007/s00018-022-04574-x

[10] S. Dervin, P. Ganguly, R. S. Dahiya, Disposable Electrochemical Sensor Using Graphene Oxide-Chitosan Modified Carbon-Based Electrodes for the Detection of Tyrosine, *IEEE Sensors Journal* **21** (2021) 26226-26233. https://doi.org/10.1109/JSEN.2021.3073287

[11] Z. Xu, X. Qiao, R. Tao, Y. Li, S. Zhao, Y. Cai, X. Luo, A wearable sensor based on multifunctional conductive hydrogel for simultaneous accurate pH and tyrosine monitoring in sweat, *Biosensors and Bioelectronics* **234** (2023) 115360. https://doi.org/10.1016/j.bios.2023.115360

[12] E. Vaughan, C. Santillo, M. Setti, C. Larrigy, A.J. Quinn, G. Gentile, M. Lavorgna, D. Iacopino, Sustainable Laser-Induced Graphene Electrochemical Sensors from Natural Cork for Sensitive Tyrosine Detection, *Advanced Sensor Research* **2** (2023) 2300026. https://doi.org/10.1002/adsr.202300026

[13] A. Afzal, F.A. Abuilaiwi, R. Javaid, F. Ali, A. Habib, Solid-state synthesis of heterogeneous $Ni_{0.5}Cu_{0.5-x}ZnxFe_2O_4$ spinel oxides with controlled morphology and tunable dielectric properties, *Journal of Materials Science: Materials in Electronics* **31** (2020) 14261-14270. https://doi.org/10.1007/s10854-020-03982-8

[14] J. Shen, S. Xu, C. Zhao, X. Qiao, H. Liu, Y. Zhao, J. Wei, Y. Zhu, Bimetallic Au@Pt Nanocrystal Sensitization Mesoporous α-Fe_2O_3 Hollow Nanocubes for Highly Sensitive and Rapid Detection of Fish Freshness at Low Temperature, *ACS Applied Materials Interfaces* **13** (2021) 57597-57608. https://doi.org/10.1021/acsami.1c17695

[15] X. Ren, J. Chen, C. Wang, D. Wu, H. Ma, Q. Wei, H. Ju, Photoelectrochemical Sensor with a Z-Scheme Fe_2O_3/CdS Heterostructure for Sensitive Detection of Mercury Ions, *Analytical Chemistry* **95** (2023) 16943-16949. https://doi.org/10.1021/acs.analchem.3c03088

[16] M. Liu, R.-Y. Sun, Y.-L. Ding, Q. Wang, P. Song, Au/α-Fe_2O_3/$Ti_3C_2T_x$ MXene Nanosheet Heterojunctions for High-Performance NH3 Gas Detection at Room Temperature, *ACS Applied Nano Materials* **6** (2023) 11856-11867. https://doi.org/10.1021/acsanm.3c01744

[17] E. Paulson, M. Jothibas, Significance of thermal interfacing in hematite (α-Fe2O3) nanoparticles synthesized by sol-gel method and its characteristics properties, *Surfaces and Interfaces* **26** (2021) 101432. https://doi.org/10.1016/j.surfin.2021.101432

[18] S. Athar, I. Zaman, A. Liaqat, A. Afzal, Disposable Saliva Sensors for Early Cancer Diagnosis Using Hyper-Cross-Linked Molecularly Imprinted Polymeric Electrocatalysts, *ACS Applied Polymer Materials* **5** (2023) 10438-10445. https://doi.org/10.1021/acsapm.3c02295

[19] R. Sen, P. Jain, R. Patidar, S. Srivastava, R. S. Rana, N. Gupta, Synthesis and Characterization of Nickel Ferrite ($NiFe_2O_4$) Nanoparticles Prepared by Sol- Gel Method, *Materials Today: Proceedings* **2** (2015) 3750-3757. https://doi.org/10.1016/j.matpr.2015.07.165

[20] Z. N. Kayani, S. Arshad, S. Riaz, S. Naseem, Synthesis of Iron Oxide Nanoparticles by Sol-Gel Technique and Their Characterization, *IEEE Transactions on Magnetics* **50** (2014) 1-4. https://doi.org/10.1109/TMAG.2014.2313763

[21] R. Malik, V.K. Tomer, S. Duhan, S. P. Nehra, P. S. Rana, One-Pot Hydrothermal Synthesis of Porous SnO2 Nanostructures for Photocatalytic Degradation of Organic Pollutants, *Energy and Environment Focus* **4** (2015) 340-345. https://doi.org/10.1166/eef.2015.1182

[22] A. Bumajdad, S. Al-Ghareeb, M. Madkour, F. A. Sagheer, Non-noble, efficient catalyst of unsupported α-Cr_2O_3 nanoparticles for low temperature CO Oxidation, *Scientific Reports* **7** (2017) 14788. https://doi.org/10.1038/s41598-017-14779-x

[23] N. Pailhé, J. Majimel, S. Pechev, P. Gravereau, M. Gaudon, A. Demourgues, Investigation of Nanocrystallized α-Fe_2O_3 Prepared by a Precipitation Process, *The Journal of Physical Chemistry C* **112** (2008) 19217-19223. https://doi.org/10.1021/jp8053313

[24] M. Hjiri, Highly sensitive NO_2 gas sensor based on hematite nanoparticles synthesized by sol-gel technique, *Journal of Materials Science: Materials in Electronics* **31** (2020) 5025-5031. https://doi.org/10.1007/s10854-020-03069-4

[25] N. A. Meyer, M. D. Wenz, J. P. S. Walsh, S. D. Jacobsen, A.J . Locock, J. W. Harris, Goldschmidtite, (K,REE,Sr)(Nb,Cr)O_3: A new perovskite supergroup mineral found in diamond from Koffiefontein, South Africa, *American Mineralogist* **104** (2019) 1345-1350. https://doi.org/10.2138/am-2019-6937

[26] X. Wang, X. Wang, Q. Di, H. Zhao, B. Liang, J. Yang, Mutual Effects of Fluorine Dopant and Oxygen Vacancies on Structural and Luminescence Characteristics of F Doped SnO_2 Nanoparticles, *Materials* **10** (2017) 1398. https://doi.org/10.3390/ma10121398

[27] Y. Li, Z. Wang, R. Liu, Superparamagnetic α-Fe_2O_3/Fe_3O_4 Heterogeneous Nanoparticles with Enhanced Biocompatibility, *Nanomaterials* **11** (2021) 834. https://doi.org/10.3390/nano11040834

[28] L. Chen, Y. Wu, N. T. H. Nhung, C. He, H. Chen, G. Dodbiba, A. Otsuki, T. Fujita, High Gradient Magnetic Separation of Pure Gd_2O_3 Particles from Pure La_2O_3 Particles, *Metals* **13** (2023) 241. https://doi.org/10.3390/met13020241

[29] S. Chen, D. Liu, N. Song, C. Wang, X. Lu, Promoting non-enzymatic electrochemical sensing performance toward glucose by the integration of conducting polypyrrole with metal-organic framework, *Composites Communications* **30** (2022) 101074. https://doi.org/10.1016/j.coco.2022.101074

[30] P. Deng, J. Xiao, J. Feng, Y. Tian, Y. Wu, J. Li, Q. He, Highly sensitive electrochemical sensor for tyrosine detection using a sub-millimeter electrode, *Microchemical Journal* **165** (2021) 106106. https://doi.org/10.1016/j.microc.2021.106106

[31] R. D. Crapnell, C. E. Banks, Perspective: What constitutes a quality paper in electroanalysis?, *Talanta Open* **4** (2021) 100065. https://doi.org/10.1016/j.talo.2021.100065

[32] E. P. Randviir, A cross examination of electron transfer rate constants for carbon screen-printed electrodes using Electrochemical Impedance Spectroscopy and cyclic voltammetry, *Electrochimica Acta* **286** (2018) 179-186. https://doi.org/10.1016/j.electacta.2018.08.021

[33] N. Baig, A.-N. Kawde, A novel, fast and cost effective graphene-modified graphite pencil electrode for trace quantification of L-tyrosine, *Analytical Methods* **7** (2015) 9535-9541. https://doi.org/10.1039/C5AY01753J

[34] T. Maiyalagan, J. Sundaramurthy, P. S. Kumar, P. Kannan, M. Opallo, S. Ramakrishna, Nanostructured α-Fe_2O_3 platform for the electrochemical sensing of folic acid, *Analyst* **138** (2013) 1779-1786. https://doi.org/10.1039/C3AN00070B

[35] E. F. Douglass Jr., P. F. Driscoll, D. Liu, N. A. Burnham, C. R. Lambert, W. G. McGimpsey, Effect of Electrode Roughness On the Capacitive Behavior of Self-Assembled Monolayers, *Analytical Chemistry* **80** (2008) 7670-7677. https://doi.org/10.1021/ac800521z

[36] H. Essousi, H. Barhoumi, S. Karastogianni, S. T. Girousi, An Electrochemical Sensor Based on Reduced Graphene Oxide, Gold Nanoparticles and Molecular Imprinted Over-oxidized Polypyrrole for Amoxicillin Determination, *Electroanalysis* **32** (2020) 1546-1558. https://doi.org/10.1002/elan.201900751

[37] I. Soni, G. Kudur Jayaprakash, A short review on the analysis of the adsorptive behavior of surfactants at carbon paste electrodes for electrochemical sensing, *Journal of Molecular Liquids* **388** (2023) 122737. https://doi.org/10.1016/j.molliq.2023.122737

[38] Y. Luo, J. Liu, X. Zhang, Z. Li, Graphene and Chitosan Composite Film Modified Electrode as a Sensitive Voltammetric Sensor for Tyrosine Detection in Food and Biological Samples, *Journal of The Electrochemical Society* **169** (2022) 016502. https://doi.org/10.1149/1945-7111/ac425b

[39] L. Fiore, B. De Lellis, V. Mazzaracchio, E. Suprun, R. Massoud, B. M. Goffredo, D. Moscone, F. Arduini, Smartphone-assisted electrochemical sensor for reliable detection of tyrosine in serum, *Talanta* **237** (2022) 122869. https://doi.org/10.1016/j.talanta.2021.122869

[40] J. Chen, Y. Chen, S. Li, J. Yang, J. Dong, X. Lu, MXene/CNTs/Cu-MOF electrochemical probe for detecting tyrosine, *Carbon* **199** (2022) 110-118. https://doi.org/10.1016/j.carbon.2022.07.021

[41] X.-Q. Wu, P.-Q. Feng, Z. Guo, X. Wei, Water-Stable 1D Double-Chain Cu Metal-Organic Framework-based Electrochemical Biosensor for Detecting l-Tyrosine, *Langmuir* **36** (2020) 14123-14129. https://doi.org/10.1021/acs.langmuir.0c02799

[42] M. Liu, J. Lao, H. Wang, Z. Xu, J. Li, L. Wen, Z. Yin, C. Luo, H. Peng, Electrochemical Determination of Tyrosine Using Graphene and Gold Nanoparticle Composite Modified Glassy Carbon Electrode, *Russian Journal of Electrochemistry* **57** (2021) 41-50. https://doi.org/10.1134/S1023193520110063

[43] C. Varodi, F. Pogăcean, M. Coroş, A. Ciorîță, S. Pruneanu, Electrochemical L-Tyrosine Sensor Based on a Glassy Carbon Electrode Modified with Exfoliated Graphene, *Sensors* **22** (2022) 3606. https://doi.org/10.3390/s22103606

[44] K. Murtada, R. Salghi, A. Ríos, M. Zougagh, A sensitive electrochemical sensor based on aluminium doped copper selenide nanoparticles-modified screen printed carbon electrode for determination of L-tyrosine in pharmaceutical samples, *Journal of Electroanalytical Chemistry* **874** (2020) 114466. https://doi.org/10.1016/j.jelechem.2020.114466

[45] Z.-Y. Li, D.-Y. Gao, Z.-Y. Wu, S. Zhao, Simultaneous electrochemical detection of levodapa, paracetamol and l -tyrosine based on multi-walled carbon nanotubes, *RSC Advances* **10** (2020) 14218-14224. https://doi.org/10.1039/D0RA00290A

[46] S. Sam, M.R. Mathew, K.G. Kumar, A Simple Electropolymer Based Voltammetric Sensor for the Simultaneous Determination of Melanoma Biomarkers-L-Dopa and L-Tyrosine, *Journal of The Electrochemical Society* **169** (2022) 027511. https://doi.org/10.1149/1945-7111/ac51a1

[47] A. Dinu, C. Apetrei, Development of Polypyrrole Modified Screen-Printed Carbon Electrode Based Sensors for Determination of L-Tyrosine in Pharmaceutical Products, *International Journal of Molecular Sciences* **22 (**2021) 7528. https://doi.org/10.3390/ijms22147528